Fault detection from guided waves and tunnel surface waves of in-mine seismic data

Fault detection from guided waves and tunnel surface waves of in-mine seismic data

METHOD

We consider four surface wave attributes, highly sensitive to lateral variations, as implemented in Colombero et al. (2019) for multifold data. In summary:

- **Energy** (Nasseri Moghaddam et al., 2005) is the sum of the squared amplitudes of the seismic traces after geometrical spreading correction. Energy peaks are expected for the seismic traces recorded on low-velocity anomalies, such as faults and shear zones, as a result of the energy trapping and back reflections at the discontinuities edges.
- **Autospectrum or autospectral density** (Zerwer et al., 2005) is the sum of the squared real and imaginary values of the Fourier transform at each frequency. Consequently, it displays the distribution of the energy content at different frequencies/wavelengths, supporting the previous attribute interpretation and also providing a rough indication on the depth of the detected anomalies.
- **Energy decay exponent** $\boldsymbol{\gamma}$ (Bergamo and Socco, 2014) is the exponents that relates the offset and energy ratios of two subsequent recordings as:
$$\frac{E_{i+1}}{E_i} = \left(\frac{r_{i+1}}{r_i}\right)^{-\gamma}, \quad (1)$$
where E_i and r_i are the energy attribute and the distance from the source for the *i*th trace. Strong deviation of γ from zero indicates energy decay or concentration caused by the lateral heterogeneity. The energy decay exponent is computed for trace windows having both positive and negative offsets. In presence of lateral discontinuities, they are expected to show marked opposite oscillations at the lateral interface linked to the direction of wave propagation. In particular, energy concentrations can be observed passing from high-velocity to low-velocity materials, whereas energy decays are expected going through the opposite material contrast.
- **Attenuation coefficient** $\boldsymbol{\alpha_f}$ (Bergamo and Socco, 2014) shows the attenuation of seismic wave at each frequency f and can be computed from the decomposed energy attributes of the two subsequent traces as:
$$E_{f,i+1} = E_{f,i} e^{-2\alpha_f (r_{i+1} - r_i)}. \quad (2)$$
Stacking the results (in absolute value) for positive and negative offsets, a clear delineation of the lateral discontinuity position can be obtained.

SYNTHETIC MODEL AND NUMERICAL SIMULATION

We created a 3D synthetic model based on the physical and elastic properties of a hypothetical deep mine. The model is 1000 m × 500 m × 500 m in x, y and depth directions, respectively. The tunnel is an 8 m × 8 m rectangular horizontal tunnel in the centre of the model. The model includes 1 m of EDZ around the tunnel and a 5-m thick dipping fault (45° from the horizontal plane) crossing the tunnel. The properties of the background homogenous environment, EDZ and fault are provided in Table 1.

	VS (m/s)	VP (m/s)	Density (kg/m^3)
Background	2700	4450	2800
EDZ	2360	3850	2600
Fault	750	1500	2200

Table 1: The elastic parameters of the synthetic model. The properties of the tunnel are selected equal of air.

In Figure 1a, we show the vertical section of the S-wave velocity model along the tunnel at y = 250 m. In Figure 2, we show a zoomed view (for better visualization of EDZ) of a horizontal section for S-wave velocity at depth 250 m.

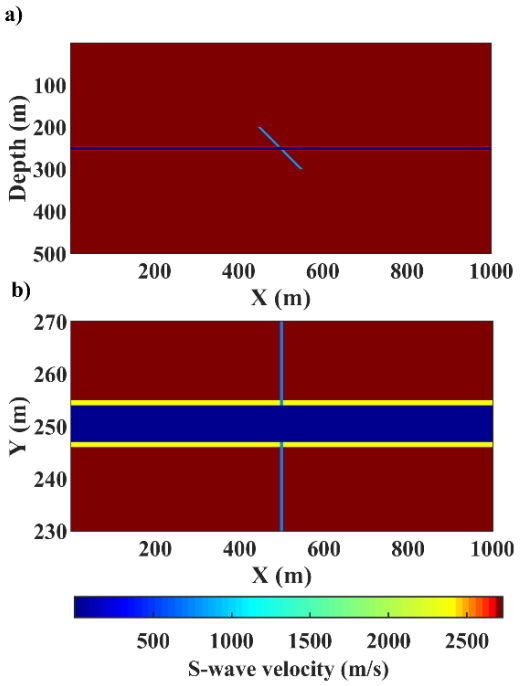

Figure 1. Slices of the S-wave velocity of the 3D synthetic model. (a) x-depth plane at y = 250 m. (b) x-y plane at depth = 250 m. The yellow layers represent the EDZ.

We use SOFI3D, an open-source viscoelastic finite-difference algorithm (Bohlen, 2002), to simulate the 3D wave propagation in the model. The method discretises the wave equation using second-order spatial and temporal finite differences over a staggered grid (Virieux, 1986). The free surface condition along the tunnel is satisfied by imposing the properties of air to the tunnel volume and without explicitly defining free surface conditions across the boundaries of the tunnel (Bohlen and Saenger, 2006). No additional free surfaces

are imposed, and the model boundaries are simulated as absorbing boundaries to avoid back reflections from the model edges.

We use grid size of 1 m in each direction, that is small enough to mitigate numerical dispersion. The time step for the finite difference computation is selected as 0.1 ms to honour the Courant-Friedrich-Lewey criterion and maintain stability. We imposed constant quality factors (Q_p and Q_s) equal to 1000, considering spatially invariant intrinsic attenuation.

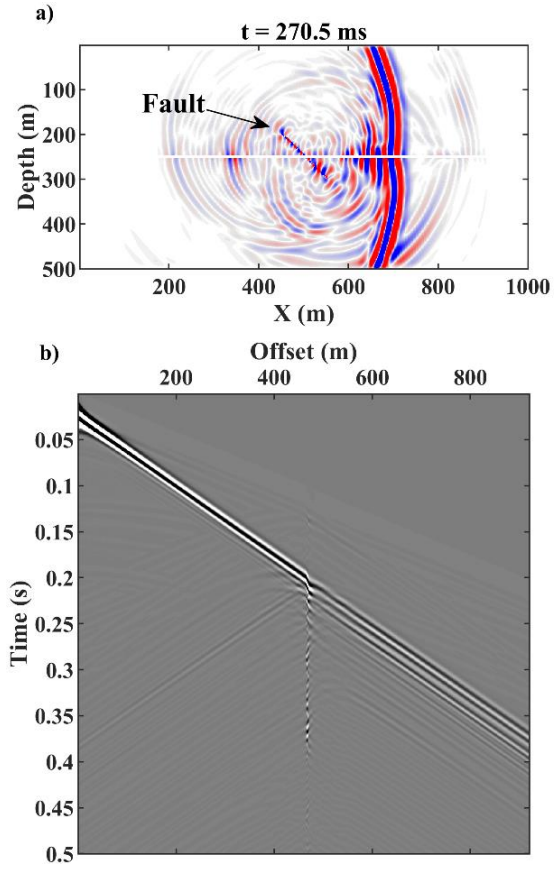

Figure 2. (a) Snapshot of the wave propagation on the x-depth plane at y=250 m and time equal to 270.5 ms. (b) Vertical component of the recorded data on the tunnel floor array. Both plots are from the shot located at X= 40 m.

We simulate a seismic experiment with a line of receivers on the floor and one on the ceiling of the tunnel and a set of shot points on the tunnel floor. We define four locations (X = 40 m, 347 m, 654 m and 961 m) on the floor of the tunnel to impose vertical point source (65-Hz Ricker wavelet). The three displacement velocity components are recorded at 920 receiver locations on the floor and 920 receiver locations on the ceiling. The receiver arrays start at X= 41 m up to X=960 m with 1 m inter-receiver spacing. Here, we only consider the vertical component to compute the attributes. The data are recorded with 0.5 ms sampling interval for a duration of 0.5 s. In Figure 2a, we show a snapshot of the vertical displacement velocity after 270.5 ms from shooting. A significant amount of energy is trapped within the fault area. In Figure 2b, we show the vertical component of the data recorded by the receivers from the same shot location as Figure 1b (X = 40 m). The data are significantly attenuated after passing through the fault (~offset 460 m).

RESULTS

In Figure 3, we show the estimated attributes on the tunnel floor and ceiling arrays, zoomed on the centre of the line (X= 400 m–600 m), close to the fault location.

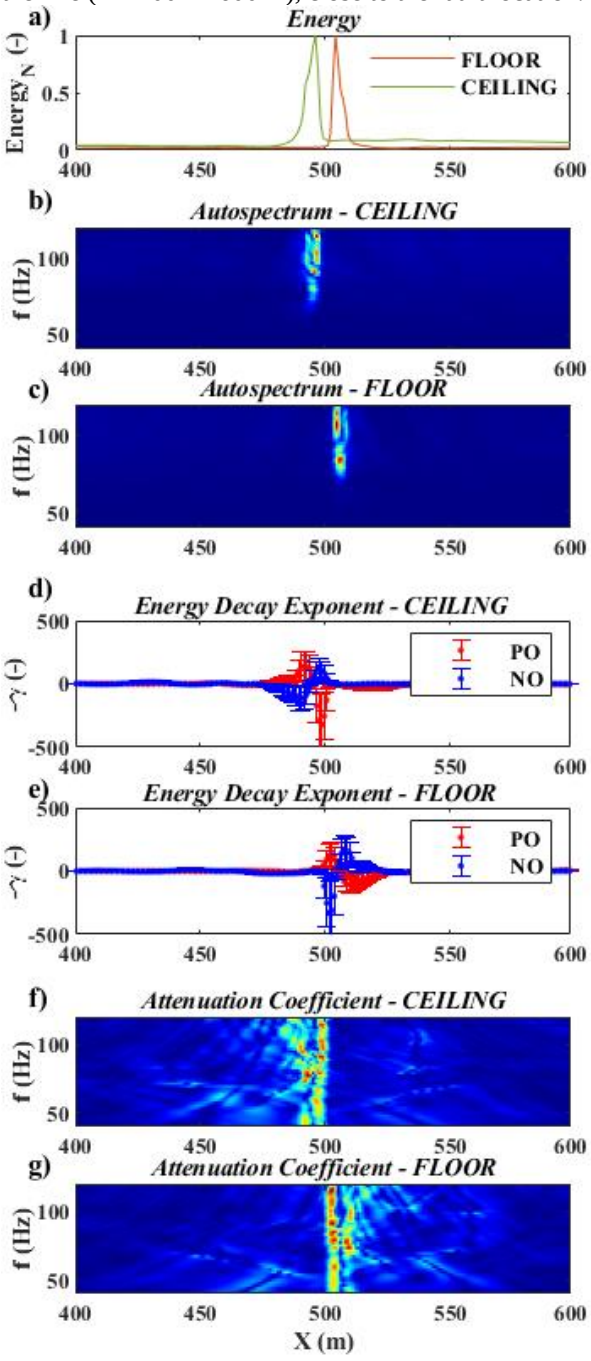

Figure 3. The estimated attributes for the synthetic data set between positions 400 m and 600 m using the floor and ceiling receiver arrays. (a) Energy attributes of floor and ceiling array. (b) and (c) Autospectrum of the ceiling and floor arrays. (d) and (e) Energy decay exponent of the ceiling and floor arrays. (f) and (g) Attenuation coefficient of the ceiling and floor arrays.

The estimated energy attribute for the floor and the ceiling are shown in Figure 3a, whereas the autospectrum attribute, energy decay coefficient and attenuation attributes are plotted separately for the floor and ceiling arrays (Figures 3b to g). All attributes, show high amplitude in the proximity of the fault location and values close to zero elsewhere. The energy attribute provides a sharp increase at the fault location along each array, as expected for anomalies having lower velocity than surrounding materials (Figure 3a). The autospectrum coherently shows two high energy spikes within the fault zone for frequencies higher than 65 Hz (Figures 3b and c). Similarly, the energy decay exponents (Figures 3d and e) show significant changes in $-\boldsymbol{\gamma}$ value. We plot the values of $-\boldsymbol{\gamma}$ such that the maxima correspond to energy concentrations and the minima correspond to energy decays. Positive and negative offset curves correspond to spatial windows located at the right and left sides respectively of each shot positions. Along both arrays, energy concentrations can be observed passing from the intact rock to the fault zone, whereas energy decays are depicted in the opposite direction.
The stacked attenuation coefficients (Figures 3f and 3g) suggest strong attenuation within a significant frequency range. The frequency band affected by the anomaly is maximum at the location of the fault crossing the array, while it decreases on opposite sides for the floor and ceiling arrays.
Comparing the floor and ceiling attributes, there is a slight but systematic shift in the position of the attribute anomalies. This shift is linked to the dip of the fault and to the fact that it intersects the tunnel at different locations on the floor and ceiling (Figure 1a and points A and B in Figure 4).

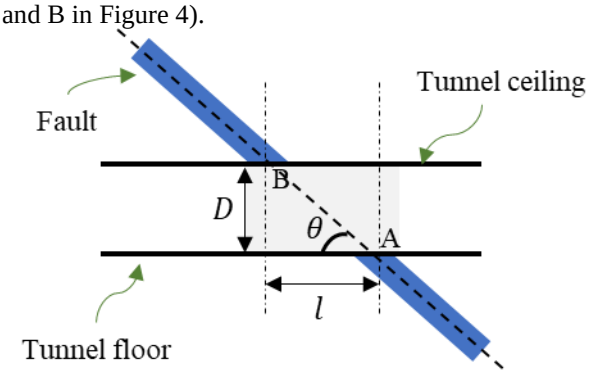

Figure 4. Schematic view of a dipping fault crossing the mining tunnel. An illustration why the attributes from the floor and ceiling receiver arrays depict the faults at different location.

We use the shift in the attribute plots and the height of the tunnel (l and D in Figure 4) to estimate the fault dip Since the shift between the floor and ceiling attributes is sharper and easy to identify in the energy plot (Figure 3a), we pick the position of the energy attribute maxima, which are at positions 496 m (ceiling, B in Figure 4) and 504 m (floor, A in Figure 4). Then, we use the distance of 8 m between the peaks to estimate the fault dip as:

$$\theta = \tan^{-1}(\frac{D}{l}). \quad (3)$$

Given that the height of the tunnel is 8 m, a θ (Figure 4) of 45° is obtained from equation 3, which exactly matches the true angle of the simulated fault.

CONCLUSIONS

Surface wave attributes have been proven to be very useful in detecting and locating lateral anomalies in on-surface seismic surveys. Here, we showed that the same attributes can be applied to in-mine seismic data not only to quickly identify the presence of faults crossing the tunnel but also to potentially predict their dip. The attributes can be applied directly to raw data and show good potential for fast and reliable screening of the tunnel walls. Nevertheless, more synthetic tests with different noise levels and real tests will be performed to evaluate the efficiency of the method in complex structural and geological environments. In future works, we also aim at analysing, discriminating, and inverting the dispersion curves of the tunnel surface wave and guided wave to obtain the S-wave and P-wave velocity models in the proximity of the tunnel, for a comprehensive characterization of the materials in support to mining exploration.

ACKNOWLEDGMENTS

This research is funded by FUTURE project of ERA-NET Cofund on Raw Materials (ERA-MIN3).
Computational resources were provided by hpc@polito, which is a project of Academic Computing within the Department of Control and Computer Engineering at the Politecnico di Torino.

REFERENCES

Bergamo, P., and Socco, L.V., 2014, Detection of sharp later discontinuities through the analysis of surface-wave propagation: Geophysics, 79, 77–90

Bohlen, T., 2002, Parallel 3-D viscoelastic finite difference seismic modelling: Computers & Geosciences, 28, 887-899.

Bohlen, T. and Saenger E.H., 2006, Accuracy of heterogeneous staggered-grid finite-difference modeling of Rayleigh waves: Geophysics, 71, 109-115

Boiero, D., and Socco, L.V., 2011, The meaning of surface wave dispersion curves in weakly laterally varying structures: Near Surface Geophysics, 9, 561–570

Colombero, C., Comina, C., and Socco L.V., 2019, Imaging near-surface sharp lateral variations with surface-wave methods—Part 1: Detection and location, Geophysics, 84, 93-111

Eales, H.V. and Cawthorn, R.G., 1996, The Bushveld complex: Developments in Petrology, 15, 181-229

Nasseri-Moghaddam, A., Cascante, G., and Hutchinson, J., 2005, A new quantitative procedure to determine the location and embedment depth of a void using surface waves: Journal of Environmental and Engineering Geophysics, 10, 51–64.

Papadopoulou, M., Colombero, C., Staring, M., Singer, J., Eddies, R., Fliedner, M., Janod, F., and Socco, L.V., 2021, Fast near-surface investigation with surface-wave attributes: 2nd Conference on Geophysics for Infrastructure Planning, Monitoring and BIM, Held at Near Surface Geoscience Conference and Exhibition.

Rapetsoa, M.K., Manzi, M.S.D., Westgate, M., Sihoyiya, M., James, I., Onyebueke,E., Kubeka, P., Durrheim, R.J., and Kgarume, T., 2022: Cost-effective in-mine seismic experiments to image platinum deposits and associated geological structures at Maseve platinum mine, South Africa, Near Surface Geophysics.

Virieux, J., 1986, P-SV Wave Propagation in Heterogeneous Media: Velocity-Stress Finite-Difference Method: Geophysics, 51, 889-901.

Zerwer, A., Polak, M.A., and Santamarina, J.C., 2005, Detection of surface breaking cracks in concrete members using Rayleigh waves: Journal of Environmental and Engineering Geophysics, 10, 295–306